

Gyrokinetic continuum simulations of plasma turbulence in the Texas Helimak

T.N. Bernard,^{1,*} E.L. Shi,^{2,3} K. Gentle,¹ A. Hakim,⁴ G.W. Hammett,⁴ T. Stoltzfus-Dueck,⁴ and E.I. Taylor¹

¹*Institute for Fusion Studies, University of Texas at Austin, Austin, TX, 78712, USA*

²*Lawrence Livermore National Laboratory, Livermore, California 94550, USA*

³*Department of Astrophysical Sciences, Princeton University, Princeton, New Jersey 08544, USA*

⁴*Princeton Plasma Physics Laboratory, Princeton, New Jersey 08540, USA*

The first gyrokinetic simulations of plasma turbulence in the Texas Helimak device, a simple magnetized torus, are presented. The device has features similar to the scrape-off layer region of tokamaks, such as bad curvature-driven instabilities and sheath boundary conditions on the end plates, which are included in these simulations. Comparisons between simulations and measurements from the experiment show similarities, including equilibrium profiles and fluctuation amplitudes that approach experimental values, but also some important quantitative differences. Both experimental and simulation results exhibit turbulence statistics that are characteristic of blob transport.

I. INTRODUCTION

In magnetically confined fusion devices such as tokamaks, the scrape-off layer (SOL) lies outside the last closed magnetic flux surface and consists of open magnetic field lines that intersect material walls. This region is characterized by fast transport along field lines toward the divertor plates or limiters and turbulent cross-field transport across field lines to the wall. Based on current experiments, the SOL heat-flux width is expected to be very narrow (only several gyroradii) and may not scale with machine size.^{1,2} Increasing turbulence could mitigate this by diffusing the power over a wider area. Also, turbulent coherent structures called blobs (also referred to as filaments),^{3–9} with higher temperatures and densities than the background plasma, are convected across field lines in the SOL and can collide with chamber walls before reaching the divertor plate, potentially damaging plasma-facing components and injecting impurities into the core plasma.¹⁰ Thus, the balance between parallel and cross-field transport in the SOL plays an important role in determining how heat and particles are exhausted in advanced fusion devices,^{11,12} and accurate modeling of this region is essential to predict the performance of future fusion reactors such as ITER.

The SOL in tokamaks is generally characterized by steep temperature and density gradients, geometry that includes an X-point, and complex physics, such as plasma-wall interactions, impurity transport, radiation, neutral recycling, and a plasma sheath. Basic plasma physics experiments with simpler magnetic configurations and lower temperature plasmas than tokamaks permit more comprehensive probe diagnostics and wider parameter scans than is generally available in fusion devices and are, thus, useful for validating analytical and numerical models of the SOL. For example, simple magnetized tori (SMT) experiments, such as the Texas Helimak^{13,14} and TORPEX,^{15–17} use vertical and toroidal field coils to create open, helical magnetic-field-line configurations

with curvature and shear. With dimensionless parameters and magnetic geometry similar to the SOL (see table 2.3 in Ref. 18), the Helimak can be used to compare analytic and numerical models of SOL turbulence with experimental data as has been done with various fluid codes.^{17,19–22}

The main turbulent drives in the Helimak are the interchange and drift wave instabilities.^{13,14,18,23} Li *et al.* developed Helimak simulations to study these instabilities using an electrostatic drift-reduced Braginskii model with cold ions.^{19,20} These fluid models produced some key experimental features, and more complete fluid models may explain SMT and tokamak-SOL plasmas well in some collisional parameter regimes. However, kinetic models are required to capture effects that can be significant in lower-collisionality parameter regimes, such as trapped particles, some non-linear wave-particle interactions, and non-Maxwellian features in the particle distribution functions.^{24–26} This paper details the first kinetic simulations of the Helimak. We use the Gkeyll computational framework to solve a five-dimensional (three spatial dimensions and two velocity dimensions) gyrokinetic equation, building on work by Shi *et al.* using straight and helical open-field-line configurations.^{27–30} We maintain similarities with the set-up of the fluid simulations in Refs. 19 and 20 for comparison with those results.

In Refs. 29 and 30, Gkeyll simulations were performed with SMT geometry and NSTX-SOL parameters for a thin radial region ($\Delta R/R \sim 0.1$). These simulations neglected geometrical variation of SOL flux surfaces with poloidal angle, such as flux expansion and magnetic shear. Other physical effects were neglected, and, therefore, detailed comparisons with experimental data were not included, though there were interesting qualitative similarities. Here we use Gkeyll to model the Helimak, where the geometry of the simulation is much closer to that in the experiment, which only has a toroidal magnetic field plus a vertical magnetic field. The experiment has some magnetic shear^{13,18} that is ignored at present in the simulation. The Helimak simulation also spans a much broader range of radius, $\Delta R/R \sim 0.5$. We include detailed comparisons with experimental measure-

* tnbernard@utexas.edu

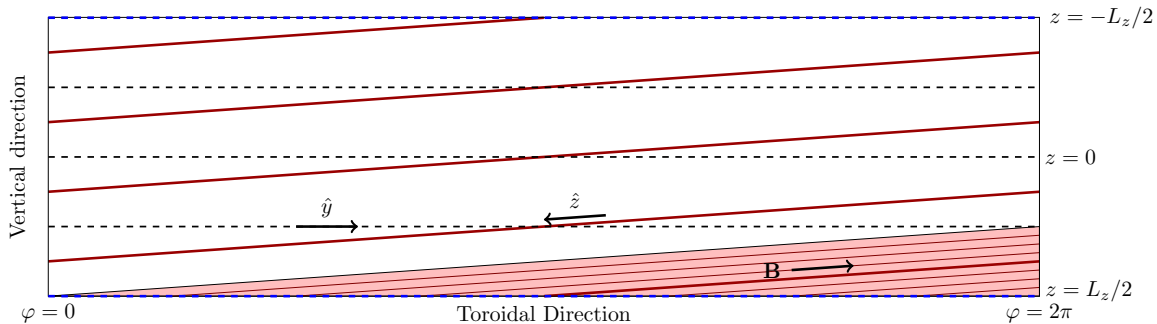


FIG. 1. A map of the non-orthogonal field-line-following coordinates to the lab frame at a slice in the radial direction for a field line with $N = 4$ toroidal turns. (The experiment we simulated has $N = 5.8$ turns.) The pink region shows the beginning of the simulation domain, starting from $z = -L_z/2$. Red lines are surfaces of constant y , which follow field lines. Additionally, y is constant on a field line. As such, it is a field line label and is used as a perpendicular coordinate. The y surfaces are shown with more frequency in the shaded region to indicate the finer resolution in y . The thick red line is parallel to the magnetic field line at $y = 0$. Dashed black lines are surfaces of constant z , with conducting sheath boundary conditions applied along the blue dashed lines, and fewer are shown to indicate the coarser resolution in z . Note that the Helimak experimental magnetic field \mathbf{B} points in the $-\hat{z}$ direction.

ments, including the time-averaged density and temperature profiles, turbulence fluctuation amplitudes, and correlation functions. There are interesting qualitative similarities but also some differences in the comparison. We acknowledge there are some missing physical effects in the code and discuss what could be added to improve agreement.

The helical pitch angle can be varied experimentally by changing resistance in the vertical field coils. In the high-pitch-angle configuration of SMT's, the interchange instability dominates since the parallel variation of the eigenmode is very small ($k_{\parallel} \simeq 0$), while in the low-pitch-angle configuration, with finite k_{\parallel} , the drift-interchange instability is the main turbulent drive.^{15,16,21,22} An equilibrium electric potential is set up radially in the Helimak due to the plasma response to sheath physics, producing a vertical sheared $\mathbf{E} \times \mathbf{B}$ flow. There are 4 sets of 4 conducting plates, 2 sets on the top and 2 sets on the bottom of the vacuum vessel, located 180° apart toroidally (See Figure 1 in Ref. 23). Each plate is approximately 0.1 m in width and 0.2 m in height. A bias voltage can be applied across the same plate in each set, such as the second from the low radial side, to study the effect of shear flow on turbulence suppression.^{13,20,23} We have simulated limiter-biased experiments but leave those results to a future paper.

This paper is organized as follows. In Sec. II, we review the model equations and parameters we use in our simulations. In Sec. III, we describe the results of our nonlinear simulation, make comparisons with experimental data, and identify dominant instabilities. In the last section, we summarize our findings and describe future directions of the code development to improve comparisons with experimental data.

II. MODEL EQUATIONS

The Gkeyll code uses a nodal discontinuous Galerkin computational method for the spatial discretization and an explicit third-order Runge–Kutta method to discretize in time.^{31,32} In our simulations, we solve the full- f gyrokinetic equation in the long-wavelength, zero-Larmor-radius limit using the gyrocenter distribution function $f_s(\mathbf{R}, v_{\parallel}, \mu, t)$

$$\begin{aligned} \frac{\partial \mathcal{J}_s f_s}{\partial t} + \nabla \cdot (\mathcal{J}_s \dot{\mathbf{R}} f_s) + \frac{\partial}{\partial v_{\parallel}} (\mathcal{J}_s v_{\parallel} f_s) \\ = \mathcal{J}_s C[f_s] + \mathcal{J}_s S_s, \end{aligned} \quad (1)$$

where s refers to the species. The phase-space advection velocities $\dot{\mathbf{R}} = \{R, H\}$ and $\dot{v}_{\parallel} = \{v_{\parallel}, H\}$ are defined in terms of the Poisson bracket

$$\begin{aligned} \{F, G\} = \frac{\mathbf{B}^*}{m_s B_{\parallel}^*} \cdot \left(\nabla F \frac{\partial G}{\partial v_{\parallel}} - \frac{\partial F}{\partial v_{\parallel}} \nabla G \right) \\ - \frac{1}{q_s B_{\parallel}^*} \mathbf{b} \cdot \nabla F \times \nabla G. \end{aligned} \quad (2)$$

The gyrocenter Hamiltonian is

$$H_s = \frac{1}{2} m v_{\parallel}^2 + \mu B + q_s \langle \phi \rangle_{\alpha}, \quad (3)$$

where $\langle \cdot \rangle_{\alpha}$ is the gyro-average. In the long wavelength limit, $\langle \phi \rangle_{\alpha} = \phi$. In the continuous-time limit, the DG advection scheme we use is energy-conserving. For more details of our computational scheme, see Refs. 28–30.

We solve for the electrostatic potential using the gyrokinetic Poisson equation with a linear ion polarization density

$$-\nabla \cdot \left(\frac{n_{i0}^g e^2 \rho_{s0}^2}{T_{e0}} \nabla_{\perp} \phi \right) = \sigma_g = e[n_i^g(\mathbf{R}, t) - n_e(\mathbf{R}, t)]. \quad (4)$$

The background ion guiding center density n_{i0}^g is taken to be constant in space and time. The ion sound gyroradius is defined as $\rho_{s0} = c_{s0}/\Omega_i$, with the ion sound speed $c_{s0} = \sqrt{T_{e0}/m_i}$. We also used a reduced mass ratio $m_i/m_e = 400$, which is about 180 times smaller than the actual argon ion-to-electron mass ratio but twice the ratio used in previous fluid simulations.²⁰

We use a non-orthogonal field-line-following coordinate system^{33–35} to model the helical field lines: z is the distance along the field, x is the radial coordinate, and y is the bi-normal coordinate. Field-line curvature enters through the second term in \mathbf{B}^* , which contributes terms proportional to $\nabla \times \mathbf{b} \cdot \nabla y = -1/x$. The field strength is dominated by the vacuum toroidal field; therefore, we assume $B(x) = B_0(R_0/x)$. Following the convention for field-line following coordinate systems³³, the magnetic field line direction \hat{z} points in the clockwise direction when viewed from above. The Helimak experimental magnetic field points in the counterclockwise, or $-\hat{z}$, direction.

Conducting-sheath boundary conditions^{28–30} are used in the z direction, where field-lines intersect the wall (or conducting plates), for the distribution function f . These permit local parallel current fluctuations into and out of the wall. Since we assume quasineutrality in our model, we do not resolve the Debye sheath, which contains $n_i > n_e$ and is on the order of a few Debye lengths. The wall is assumed to be just outside the simulation domain. We solve for the sheath potential ϕ_{sh} at the boundary using the gyrokinetic Poisson equation. This sets a cut-off parallel velocity for electrons, $\frac{1}{2}m_e v_c^2 = e\phi_{\text{sh}}$. Electrons with velocities greater than v_c leave the domain, while those with smaller velocities are reflected. Dirichlet boundary conditions are used in x for the potential ($\phi = 0$), and periodic boundary conditions are used in y for f and ϕ .

TABLE I. Summary of Helimak simulation parameters

Background magnetic field	$B_0 = 0.1$ T
Background density	$n_0 = 10^{16}$ m ⁻³
Background electron temperature	$T_{e0} = 10$ eV
Background ion temperature	$T_{i0} = 1$ eV
Ion sound gyroradius	$\rho_{s0} = 2.04 \times 10^{-2}$ m
Electron gyroradius	$\rho_e = 0.102 \times 10^{-2}$ m
Ion sound speed	$c_s = 4.9 \times 10^3$ m/s
Density gradient scale length	$L_n = 0.1$ m
Electron mean free path	$\lambda_{ee} = 98.4$ m
Ion mean free path	$\lambda_{ii} = 1.38 \times 10^{-2}$ m

The Helimak simulations with Gkeyll evolve the electron and ion distribution functions for an argon discharge. We chose simulation parameters based on typical experimental parameters^{13,23} and previous fluid simulations,^{19,20} using $B_0 = 0.1$ T and $n_{i0}^g = n_{e0} = 10^{16}$ m⁻³. Since the electron-ion thermal equilibration time is much longer than a charge-exchange time and particle confinement times for parallel loss, $T_{i0} \ll T_{e0}$

in the experiment. We use $T_{e0} = 10$ eV based on experimental measurements. Previous work^{14,19} estimates $T_{i0} \sim 0.1$ eV, though this has not been accurately measured. Argon that is ionized at different locations will be accelerated for different lengths of time towards the device ends by the pre-sheath potential, which varies along a field line. This will produce an ion temperature that is a significant fraction of the pre-sheath potential drop, which is of order T_{e0} . Therefore, we use $T_{i0} = 1$ eV. The equilibrium temperatures define the velocity grid and appear in the the source terms, which we explain in more detail below. The particle temperatures T_i and T_e vary spatially and are evolved self-consistently in time. See Table I for a summary of key simulation parameters.

The toroidal vacuum chamber of the Helimak is rectangular with a radial extent $0.6 \text{ m} \leq R \leq 1.6 \text{ m}$ and a vertical height $H = 2.0$ m. By changing the current through the vertical field coils, the magnetic-field-line connection length L_c can be varied from 12 m to 500 m. In our simulations, we use a slab-like metric with a spatial Jacobian that is independent of x . To simulate the entire volume of the Helimak, the configuration space extents are $x \in [0.6, 1.6]$ m and $z \in [-L_c/2, L_c/2]$. L_y varies inversely with the connection length: $L_y = H/N$, where $N = L_c/(2\pi R_0)$ is the number of field-line turns and $R_0 = 1.1$ m. This gives $y \in [-L_y/2, L_y/2]$. In the experiment, there is magnetic shear due to the variation in the field with respect to R , which is not included in this model. This also means that the connection length L_c and binormal length of periodicity L_y do not vary in x as they realistically should. The parallel velocity-space extents are given by $v_{\parallel,e} \in [-v_{e,\text{max}}, v_{e,\text{max}}]$ and $v_{\parallel,i} \in [-v_{i,\text{max}}, v_{i,\text{max}}]$, where $v_{e,\text{max}} = 4v_{te} = 4\sqrt{T_{e0}/m_e}$ and $v_{i,\text{max}} = 6c_s = 6\sqrt{T_{e0}/m_i}$. The perpendicular velocity-space extents for each species are given by $\mu_s \in [0, 3m_s v_{s,\text{max}}^2/(16B_0)]$. The grid resolution is $(N_x, N_y, N_z, N_{v_{\parallel}}, N_{\mu}) = (48, 24, 16, 10, 5)$ with uniform spacing. The numerical solutions for the distribution function and the Hamiltonian are projected onto piecewise-linear basis functions using the discontinuous Galerkin scheme. Because the gyrokinetic system is highly dimensional and computationally intensive, convergence tests were performed only in the x direction for a low-resolution, $(N_x, N_y, N_z, N_{v_{\parallel}}, N_{\mu}) = (N_x, 12, 8, 10, 5)$, and a higher-resolution, $(N_x, N_y, N_z, N_{v_{\parallel}}, N_{\mu}) = (N_x, 24, 16, 10, 5)$, case. Power in the Fourier transform in x of electron density fluctuations are compared for different resolutions in Fig. 2. Fluctuations are calculated as $\tilde{n} = n - \langle n \rangle_y$, where the last term denotes an average in the y -direction. The power has been averaged in z and in time from 10 to 16 ms. The decay of the power at high k_x indicates that the simulations are not changed significantly with increased resolution. Furthermore, equilibrium profiles and turbulence statistics were similar for the different cases.

In the Helimak, electrons are preferentially heated by electron-cyclotron and upper-hybrid resonances. The latter is believed to dominate and is localized from 1.0–

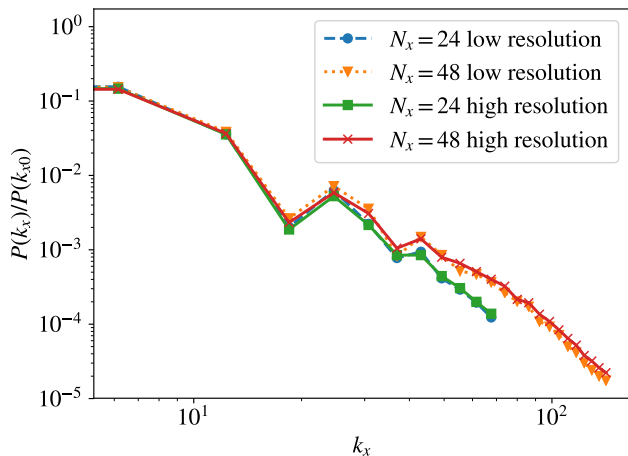


FIG. 2. Power in the Fourier transform in x of electron density fluctuations is compared for various resolutions. The power has been averaged in z and in time from 10 to 16 ms. The low resolution case has $(N_x, N_y, N_z, N_{v_{\parallel}}, N_{\mu}) = (N_x, 12, 8, 10, 5)$ and the higher resolution case has $(N_x, N_y, N_z, N_{v_{\parallel}}, N_{\mu}) = (N_x, 24, 16, 10, 5)$. The decay of the power at high k_x indicates that our simulations are not changed significantly with increased resolution.

1.1 m radially.¹⁸ The upper-hybrid resonance heating is difficult to model accurately due to its density dependence. The source is also challenging to model because the particle source rate and power deposition into the plasma are not accurately known. It is estimated that over 90% of the 6 kW input power is lost to radiation by electron-impact excitation of neutral argon. This process depends on the neutral density profile. We estimated the total radiative cooling using the predicted radiative cooling rate L_Z in Ref. 36. The total power radiated in the device is given by $P_{\text{rad}}\mathcal{V} = L_Z n_e n_{\text{imp}}\mathcal{V} \simeq 5.5$ kW, assuming $T_e = 10$ eV, $n_e = 1 \times 10^{16} \text{ m}^{-3}$, and the total Argon density (including neutrals) is $n_{\text{imp}} = 4 \times 10^{17} \text{ m}^{-3}$. \mathcal{V} is the total volume of Helimak vacuum vessel. Neutral interactions and radiation are neglected in our present source model.

We employ the simplified source model used in Refs. 28–30. For both species, we assume a source of the form

$$S_s(\mathbf{R}, v_{\parallel}, \mu) = S_0 \exp[-(x - x_{\text{src}})^2 / (2\sigma_{\text{src}}^2)] \times F_M(v_{\parallel}, \mu; T_{s,\text{src}}), \quad (5)$$

where s refers to species, F_M is a normalized, non-drifting Maxwellian, $x_{\text{src}} = 1.0$ m is the source location, and $\sigma_n = 0.01$ m is the source width. $T_{s,\text{src}}$ is the source temperature. The source is independent of y , z , and t . Previous fluid simulations use $\sigma_{\text{src}} \sim 0.1$ m. We chose a narrower source because the RF resonance probably is very narrow, though the location of the upper-hybrid resonance fluctuates as the density fluctuates. Equilibrium profiles are broadened by turbulence and wider than the

assumed source width. Low-resolution scans in σ_{src} from 0.1 to 0.01 m produced little effect on resulting equilibrium profiles.

Since the actual particle and power source rates are not well known, we estimate the particle source rate S_0 and source temperature $T_{s,\text{src}}$ using a 1D fluid transport model (see Appendix B in Ref. 29 or Appendix A in Ref. 30) to approximately produce the observed quasi-steady-state density and temperature profiles. We assume a balance of source rates and losses using

$$\frac{d\mathcal{N}}{dt} = \int d\mathbf{R} \left[S_n(x) - \frac{n(x, z)}{\tau_{\parallel}} \right] = 0, \quad (6)$$

where \mathcal{N} is the total number of particles and $\tau_{\parallel} = L_z / (2c_s)$ is the parallel transit time. We assume a steady-state density profile with a variation in z based on a 1D steady-state single fluid calculation.

$$n(x, z) = n_p \exp \left[-\frac{(x - x_{\text{src}})^2}{2\sigma_n^2} \right] \times \frac{1 + \sqrt{1 - z^2 / (L_z/2)^2}}{2}. \quad (7)$$

The peak density n_p is calculated such that $\int d\mathbf{R} n(x, z) / \mathcal{V}$ is equal to the background density. We define the density source for each species as $S_{s,n}(x) \equiv \int d\mathbf{v} S_s(\mathbf{R}, \mu, v_{\parallel})$ and use Eqns. 7 and 6 to estimate $S_0 \approx 9.77 \times 10^{19} \text{ m}^{-3}\text{s}^{-1}$ for the source amplitude. We estimate $T_{s,\text{src}} = \frac{5}{3}T_{s0}$ for the source temperature in Eq. 5 based on the temperature at the midpoint in z of a 1D steady-state fluid calculation.^{29,30} However, that model assumes only convective outflows and neglects the fast parallel thermal transport of electrons, so it was necessary to double this value for electrons ($T_{e,\text{src}} = \frac{10}{3}T_{e0}$) to approximately match experimental electron temperature profiles.

We expect the quasi-steady-state conditions of the simulation to be independent of initial conditions. Therefore, we chose initial conditions with a narrow density gradient scale length and a non-zero flow velocity as a function of the parallel coordinate, computed from simplified 1D fluid models following Ref. 29 and 30. The density initial conditions are pictured in Fig. 3. We also use a density floor of 10% to minimize unphysical negative values in our full- f distribution function. The code includes a scheme to correct for negative values of the distribution function, detailed in Refs. 28 and 29, which adds a small amount of numerical heating ($\sim 10\%$) to the simulations. (A new version of the code is under development and has a more robust method of preventing negative values of the distribution function.)

Scans of the ion-to-electron mass ratio were performed in previous helical open-field-line simulations with Gkeyll and resulted in no significant changes to turbulence statistics.^{29,30} The difference between the true and reduced mass ratio for argon is much larger in the case of the Helimak. The large parallel ion transit time requires longer simulation times to reach saturation and is computationally expensive. By solving

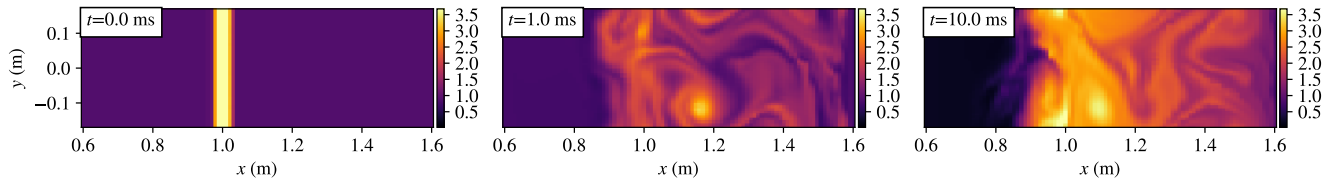


FIG. 3. These plots depict ion guiding-center density (10^{16} m^{-3}) in the field-line-following coordinate system in (x, y) at the center of the z domain ($z = 0$). Snapshots are shown at 0, 1, and 8 ms.

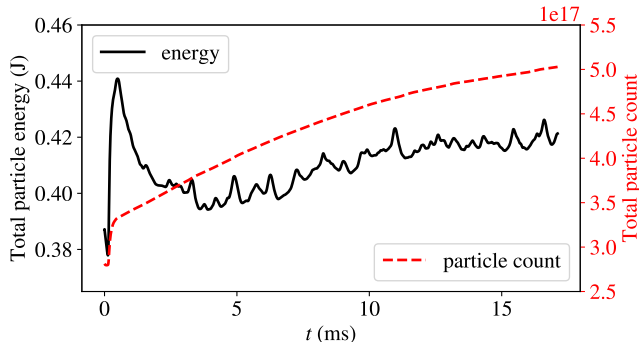


FIG. 4. A plot of the total particle count and the total particle energy in the simulation. Particle energy for a single species is calculated as the integration of the product of the particle Hamiltonian and distribution function over all phase space. Time-averaged profiles and turbulence statistics were calculated from 6 to 12 ms.

for linear perturbations in the parallel current, \tilde{j}_{\parallel} , near the sheath and using $j_{\parallel e} + j_{\parallel i} = 0$, we estimated that reduced ion-to-electron mass ratio would underpredict turbulence fluctuation levels by approximately 50%. A comparison of low-resolution simulations, $(N_x, N_y, N_z, N_{v_{\parallel}}, N_{\mu}) = (24, 12, 8, 10, 5)$, with the true and reduced mass ratio supports this prediction. A new modal discontinuous Galerkin version of Gkeyll with automatic code generation is under development and is much faster. It should allow routine use of higher mass ratios in the future.

III. SIMULATION RESULTS

We ran the simulation using the Skylake (SKX) compute nodes on the Stampede2 cluster at the Texas Advanced Computing Center. A simulation of a 16 ms argon discharge for $L_z = 40$ m required approximately 180,000 CPU-hours. This is about 4 times the ion transit time, $\tau_{\parallel} = L_z/(2c_s) = 4.084$ ms, which is the time it takes an ion traveling at its characteristic sound speed, with $T_{e0} = 10$ eV, to traverse half the magnetic-field-line connection length. We compared with experimental data from a discharge with a similar connection length at

$R_0 = 1.1$ m. The experimental connection length is varied by changing the resistance in the vertical field coils, and this simulation corresponded to a resistance of 2.7Ω . This resistance produces the lowest connection length for which field lines terminate on the conducting end plates at the bottom and top of the device. Resistance can be varied up to 25Ω , resulting in a connection length on the order of 400 m.

Figure 4 shows the total particle count and total energy ($\mathcal{E}_{\text{tot}} = \mathcal{E}_e + \mathcal{E}_i$) of the simulation. Particle energy for a single species is calculated as the integration of the product of the particle Hamiltonian and distribution function over all phase space:

$$\mathcal{E}_s = \int dz H_s f_s(\mathbf{z}). \quad (8)$$

Particle count is still increasing, though beginning to level-off by the end of the simulation. The energy appears to saturate around 10 ms. (The large spike in energy at early time is due to numerical heating added from the scheme to correct for negative distribution function values.) The nearly constant energy but increasing particle count indicates a slight decrease in temperature. We calculate equilibrium profiles and turbulence statistics over the interval from 10 to 16 ms.

In the simulation, turbulent structures develop at 0.1 ms, and a quasi-steady state is reached at approximately 4 ms. Figure 3 contains snapshots of the ion guiding-center density in the non-orthogonal field-line-following coordinate system. Using the transformation,

$$\begin{aligned} Z &= -2.0z/L_z + 1.0 \\ \varphi &= -\frac{2\pi}{L_y} \left(y + \frac{2.0z}{L_z} - 1.0 \right), \end{aligned} \quad (9)$$

this coordinate system (x, y, z) can be mapped to the lab frame (R, φ, Z) , which is shown in Fig. 5 along a slice in the toroidal coordinate φ . $N = L_z/(2\pi R_0) = 5.8$ is the number of toroidal turns of the field line. For more details of this mapping, see Fig. 1. Figure 6 depicts the ion density, electron temperature, and electrostatic potential at $t = 5$ ms in the field-line-following coordinate system at the midpoint along z .

Figure 7 compares equilibrium profiles of simulation and experimental data. Experimental Langmuir probes are located on conducting plates at the top and bottom

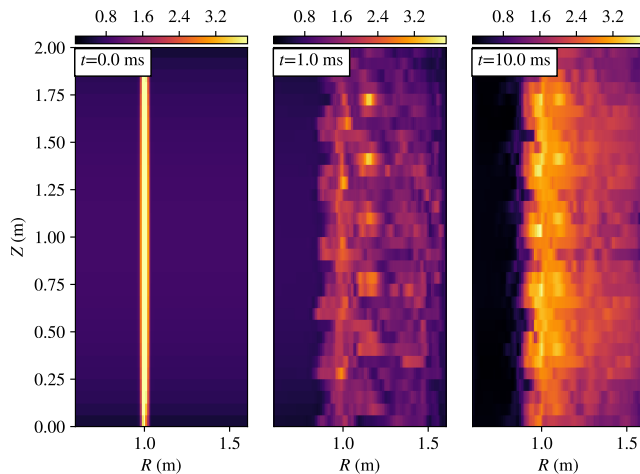


FIG. 5. These plots depict ion guiding-center density (10^{16} m^{-3}) in the lab coordinates (R, Z) at a slice in the toroidal coordinate φ . Snapshots at 0, 1, and 10 ms are shown. The vertical coordinate Z is parametrized by the magnetic field line coordinate z and is, therefore, depicted with coarser resolution.

of the vacuum vessel. The probes used to calculate equilibrium profiles have about a 50% uncertainty, and data is generally fit to a smooth curve. There is a top-bottom asymmetry in experimental density profiles. This is not present in the simulation, since our model is symmetric in z . Thus, in all comparisons we calculate simulation data at the minimum of the z domain ($z = -L_z/2$). One reason for this asymmetry could be the vertical (Z in the lab frame or z in the simulation) $\mathbf{E} \times \mathbf{B}$ drift, which we presently neglect in our model (this is a common assumption for core flux-tube codes assuming $k_\perp \gg k_\parallel$, but can break down for long wavelength components or small magnetic pitch angle). Based on experimental flow data from Ref. 23, the vertical $\mathbf{E} \times \mathbf{B}$ flow is 2–3 times the vertical component of the sonic outflows along the field lines for simulated parameters. This factor increases as the toroidal field component B_T increases relative to the vertical component B_V and may influence observed density profiles. Additionally, the microwave waveguide enters the machine at the bottom and may explain the similarity in bottom density profiles for different pitch angles which is not observed for top profiles.¹⁸ Experimental temperature profiles are fairly top-bottom symmetric and centered around 1.1 m, irrespective of pitch angle.¹⁸ Since electron parallel heat conduction is rapid, the electron-temperature steady-state profiles would be less affected by the vertical $\mathbf{E} \times \mathbf{B}$ drift or the location of the microwave guide. A full analysis of the effects of mean vertical $\mathbf{E} \times \mathbf{B}$ flows on the asymmetry in the experimental profiles involves solving a complex non-linear equation and is not within the scope of this paper.

We model the source for each species using a single

Maxwellian with a flat temperature profile and a density profile centered at 1.0 m. We chose the location of the source based on experimental steady-state density profile. Figure 7 depicts the narrow electron density source (in gray) and resulting equilibrium profiles which were broadened by turbulence. Since the net power deposition in the experiment is not well understood, we have some flexibility in our particle source rate and could further tune this parameter to achieve better agreement in the density profile magnitude. However, the gradients of the data sets match well. The simulation produced a temperature profile that was centered to the left of the experimental profile and was slightly less in magnitude and gradient-scale-length. The simulated plasma potential profile is shown in the same plot as $e\phi/\Lambda$, where $\Lambda = \ln\sqrt{m_i}/(2\pi m_e)$ for the reduced ion-to-electron mass ratio and the true mass ratio. An estimate of the simulated floating potential using $\phi_f \simeq \phi - T_e\Lambda/e$ agrees qualitatively with experimental measurements of the same quantity.^{13,18,23}

The simulated turbulence profiles come closer to experimentally measured levels than previous fluid simulations.¹⁹ Turbulence levels are calculated as the root-mean-square of electron density fluctuations, $\tilde{n} = n - \langle n \rangle$, normalized to the mean electron density $\langle n \rangle$. Experimental values have very small associated errors. In the simulation, angle brackets $\langle \rangle$ denote an average in time, performed from 10 to 16 ms, and an average in the azimuthal angle. Plot 8(a) is normalized to a local mean density, while 8(b) is normalized to a global mean density. The latter shows slightly better agreement, though both differ at large radii. This might be improved by implementing a density-weighted Poisson equation, instead of the current one (see Eq. 4) in which the background ion guiding center density n_{i0}^g is constant in space and time. This approximation is similar to the Boussinesq approximation used in many fluid models.^{19,20,37} Some simulations have relaxed this approximation^{38–40} but have not been tested with Helimak parameters.

The plasma potential equilibrium profile generates a sheared flow in the y direction. This flow is calculated as $V_E = -(d\phi_0/dx)/B_0$, with the negative sign resulting from the direction of the experimental magnetic field, and the corresponding shear as $\gamma_E = |dV_E/dx|$. We approximate the experimental flow and shear from the experimental temperature profiles by assuming $\phi_0 \approx \Lambda T_e/e$, though this calculation overestimates the flow velocities as compared with published experimental measurements.^{20,23} Previous research has shown that velocity shear in strongly magnetized plasmas has a stabilizing effect by breaking apart turbulent eddies.⁴¹ Therefore, we depict both flow and shear in Fig. 9 (a) and (b), respectively, and compare the latter to the local linear growth rate of the interchange instability $\gamma_I = c_s/\sqrt{RL_p}$. The pressure gradient scale length is defined as $1/L_p = -(dp/dx)/p$. Turbulence statistics, such as power spectra and auto-correlation functions,

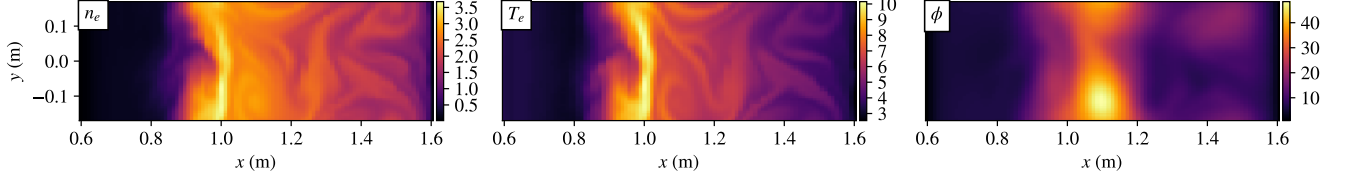


FIG. 6. These plots depict electron density (10^{16} m^{-3}), electron temperature (eV) and electrostatic potential (V) in (x, y) in the field-line-following coordinate system at the center of the z domain ($z = 0$) at $t = 8$ ms.

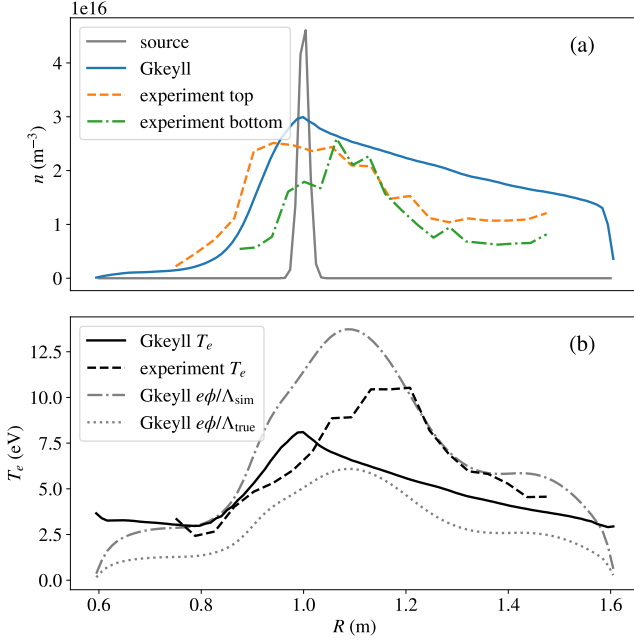


FIG. 7. Comparison of (a) the electron density profiles shown with the narrow source and (b) electron temperature profiles shown with the simulated plasma potential, assuming an adiabatic electron response. $\Lambda = \ln \sqrt{m_i / (2\pi m_e)}$, where Λ_{true} uses the real ion-to-electron mass ratio and Λ_{sim} uses the reduced ion-to-electron mass ratio of 400. $e\phi / \Lambda_{\text{sim}}$ is not exactly equal to T_e because the conducting sheath boundary condition allows currents to flow in and out of the walls. The quasi-steady state profiles are calculated by averaging simulation data in time from 10 to 16 ms and in the azimuthal angle.

are calculated at radial locations where $V_E \simeq 0$, at $R = 1.09$ m for the simulation and $R = 1.17$ m for the experiment, and where V_E is approximately maximal, at $R = 1.20$ m for the simulation and $R = 1.25$ m for the experiment.

The power spectra are calculated from the Fourier transform of the electron density fluctuations $\tilde{n} = n - \langle n \rangle$ with respect to time. Since the density fluctuations are not periodic at the boundaries t_{min} and t_{max} of this time series, we multiply the density fluctuations by a sinusoidal window prior to performing the FFT:

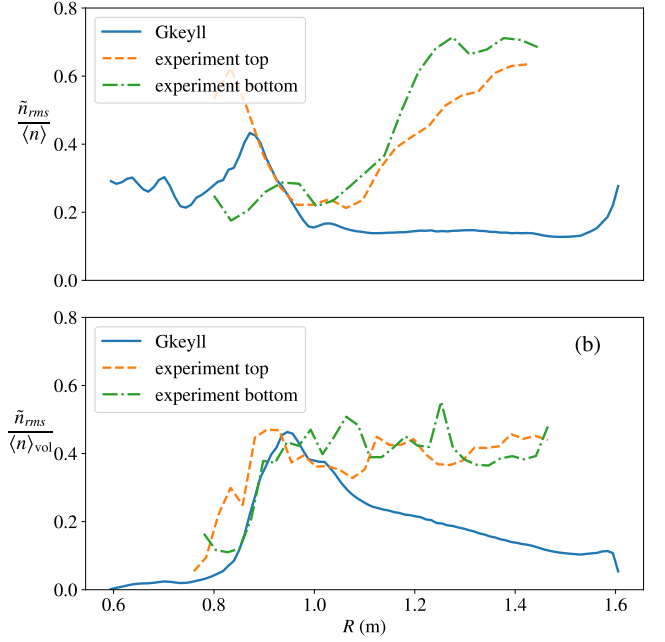


FIG. 8. Electron density fluctuation profiles depicted here are normalized to (a) the local mean density $\langle n \rangle(R)$, which is averaged in time and in the azimuthal angle and (b) normalized to volume-averaged density $\langle n \rangle_{\text{vol}}$, which is averaged in time and over the entire volume.

$$\tilde{n}_w(t_i) = \left[1 - \cos \left(\frac{2\pi}{N_t} i \right) \right] \tilde{n}(t_i). \quad (10)$$

The integer i runs from 0 to N_t , ensuring that the time series is 0 and thus periodic. The power spectra is then normalized as

$$\mathcal{P}(f) = \frac{\langle |\tilde{n}(f)|^2 \rangle}{\sum_f \Delta f |\tilde{n}(f)|^2}, \quad (11)$$

where f denotes frequency and not the distribution function. The frequency grid spacing Δf is 168 Hz. The same window and sampling frequency were used for both simulation and experimental data. The experimental data uses a longer time series and was binned to 6 ms intervals and then averaged.

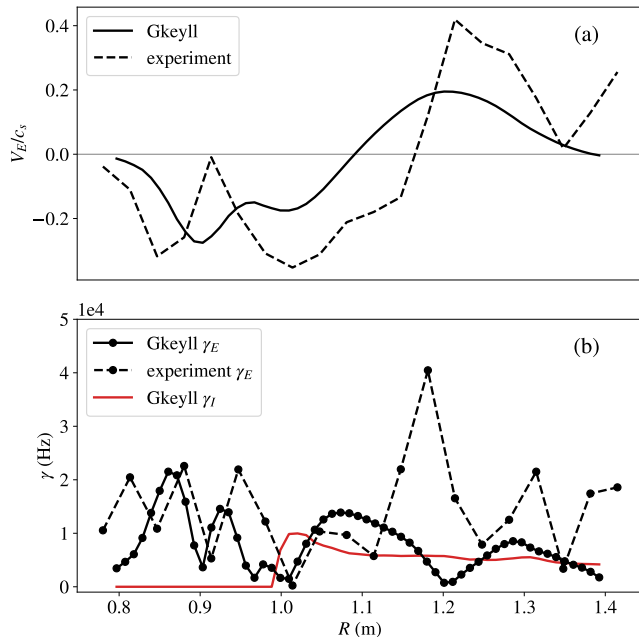


FIG. 9. Plot (a) displays the $\mathbf{E} \times \mathbf{B}$ drift velocity V_E normalized to the ion sound speed. Plot (b) displays the absolute value of the shear γ_E compared to the local interchange growth rate γ_I . The experimental velocity shear was estimated from the T_e data, assuming $\phi_0 \approx \Delta T_e/e$.

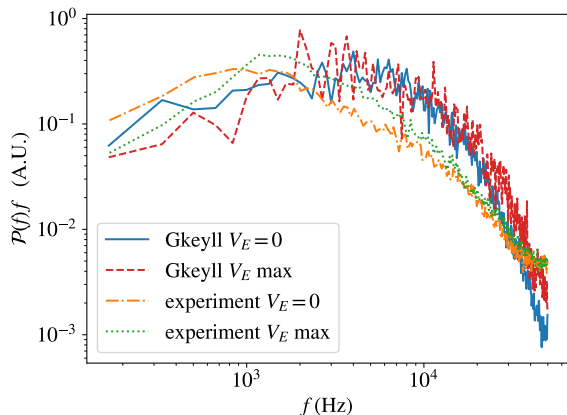


FIG. 10. Comparison of power spectra for simulation (blue and red) and experimental (orange and green) data at radial locations where V_E is zero and maximal.

Figure 10 compares the experimental and simulated power spectra multiplied by the frequency, $\mathcal{P}(f)f$, at radial locations where $\mathbf{E} \times \mathbf{B}$ flow is zero and maximal. The experimental spectra peak near 1.2 kHz, in accordance with previous results,^{14,19} while the simulation spectra peak above 2 kHz. The spectra are broader at radii where V_E is maximal compared with spectra at radii where V_E is zero. This is consistent with previous studies of turbu-

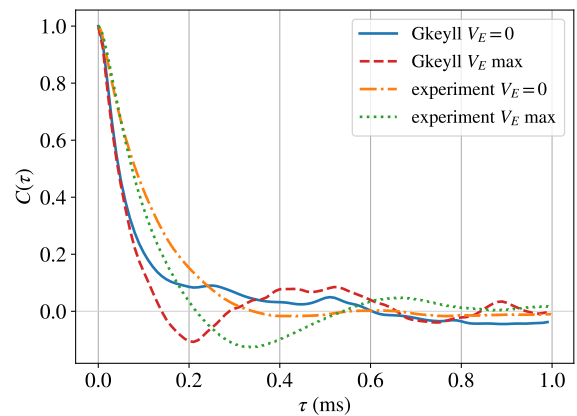


FIG. 11. Comparison of autocorrelation functions for simulation (blue and red) and experimental (orange and green) data at radial locations where V_E is zero and maximal.

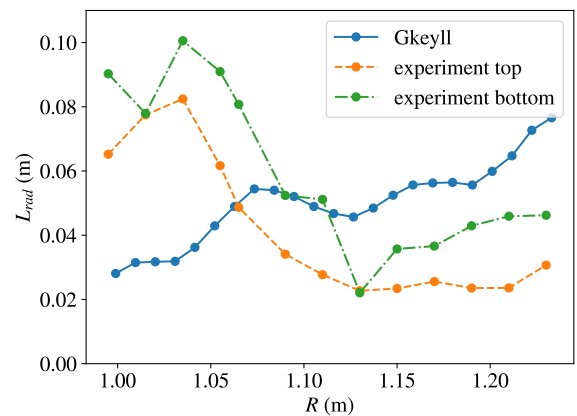


FIG. 12. Radial correlation lengths L_{rad} as a function of radius are compared for the simulation and experiment.

lence in this regime.⁴² Overall, the experimental spectra are broader at higher frequencies, a key feature of random fluctuations.⁴² Other turbulence statistics indicate stronger oscillatory behavior in the simulation fluctuations.

Figure 11 depicts the autocorrelation functions, which are calculated as $C(\tau) = \langle \tilde{n}(t)\tilde{n}(t+\tau) \rangle / \langle \tilde{n}(t)^2 \rangle$. Brackets denote a time average, and τ is the time difference. In both sets of data, the curves where V_E is maximal exhibit more oscillatory behavior, though the correlation time for the simulation data is shorter. The peak for the simulation spectra at the maximal V_E radial location is 2.3 kHz, and the inverse corresponds to approximately 0.43 ms, satisfying the Wiener-Khinchine theorem.^{43,44} The other sets of data also satisfy this theorem.

Figure 12 compares the radial correlation length as a function of radius. There is good agreement near $R = 1.1$ m, where the simulation connection length is the same

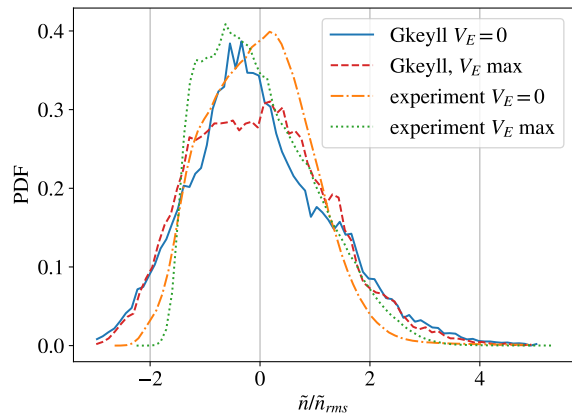


FIG. 13. Probability density functions for density fluctuations normalized to the root-mean-square. Experimental and simulation data are compared where V_E is zero and maximal.

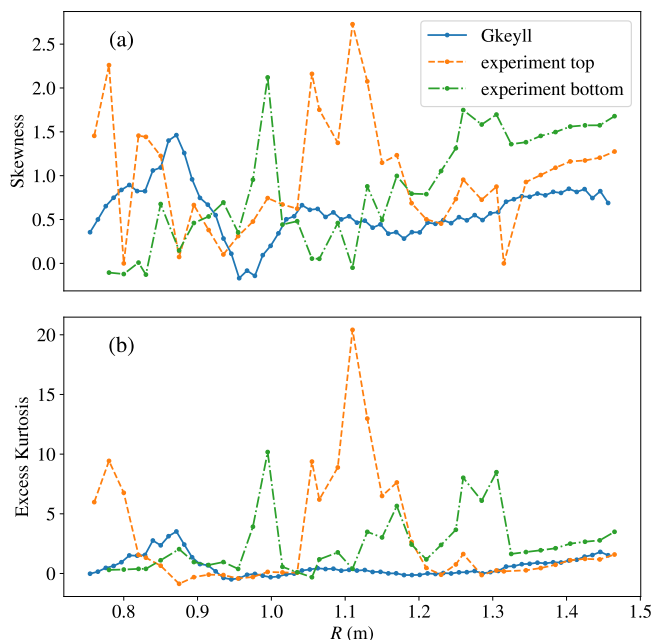


FIG. 14. Comparison of (a) skewness and (b) excess kurtosis of density fluctuations as a function of radius for simulation and experimental values.

as the experiment, but there are differences elsewhere. Furthermore, reduced turbulence levels have been shown to correspond to a reduction in the radial correlation length.^{23,41} However, the correlation lengths are larger for the simulation at $R > 1.1$ m, though the turbulence fluctuations are less than experiment in this region.

Figure 13 compares the probability density functions (PDF's) at radial locations where V_E is zero and maximal. Experimental values were measured at the bottom of the device and calculated as $\tilde{n}/\tilde{n}_{rms}$. In figure

14(a) experimental and simulation density fluctuations exhibit positive skewness, which is a characteristic of blob transport,⁴⁵ though experimental values are higher than the simulation at large radii. Skewness is calculated as $E[\tilde{n}^3]/\sigma^3$, where $E[\dots]$ is the expectation value and σ is the standard deviation of the density fluctuations. We compare excess kurtosis in Fig. 14(b), which is calculated as $E[\tilde{n}^4]/\sigma^4 - 3$. This comparison indicates that the simulation slightly underpredicts the positive excess kurtosis of the experiment, another signature of blob transport.⁴⁵ Values of skewness and kurtosis from Gkeyll simulations with NSTX-like parameters were higher than those calculated here.^{29,30}

Figure 15 shows a plot of the electron density (x, z) at the midpoint in y , and there is little structure in z in the bad curvature region $R > 1.0$ m. This suggests interchange-like, or $k_z \approx 0$, turbulence. Figure 16 depicts a Fourier transform of the density fluctuations ($\tilde{n} = n - \langle n \rangle_y$) in z , averaged in x and y and in time from 10 to 16 ms. The power of the first four modes of k_z are shown in (x, y) . The zeroth mode is over ten times greater than the other modes, suggesting that the $k_z = 0$ mode dominates. Limitations in computational resources prevented high-resolution comparisons with lower pitch angles, particularly because the parallel ion transit times are longer and require longer simulation times to saturate. Low-resolution test cases demonstrated greater k_z structure as the pitch angle was decreased, possibly indicating a transition to the drift-interchange-driven turbulence regime as predicted in Refs. 16 and 22.

IV. CONCLUSION

This work represents the first extensive comparison of kinetic simulations of a toroidal open-field line basic plasma physics device with experimental data. The results demonstrate good progress towards modeling turbulence on helical open-field lines in tokamak SOL-like conditions with gyrokinetic equations. They capture features of the Texas Helimak experimental equilibrium profiles, such as the magnitude and gradient scale lengths, and turbulence fluctuation levels are closer to experiment than previous fluid simulations. Qualitative features of turbulence statistics were also captured, such as oscillations in the autocorrelation function where V_E is maximal, radial correlation lengths of similar magnitude, and positive skewness and excess kurtosis of the distribution function in the bad curvature region. Previous research suggests that interchange turbulence should dominate for this connection length, and this is confirmed with $k_{\parallel} \approx 0$ in our simulations. However, it is clear that key physical and geometric features are still required in our model for better overall agreement with experimental turbulence statistics.

A more self-consistent source model that includes radiation and the density-dependent upper-hybrid resonance might improve the agreement of equilibrium

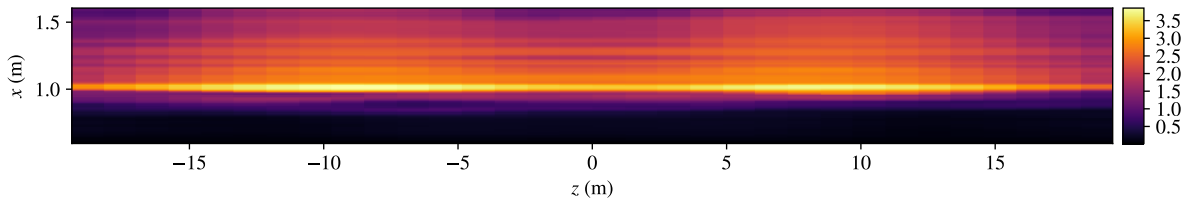


FIG. 15. Snapshot of electron density $n_e(x, y = 0, z)$ at the midplane in y at 10 ms shows little structure along z . (Aspect ratio is not to scale.)

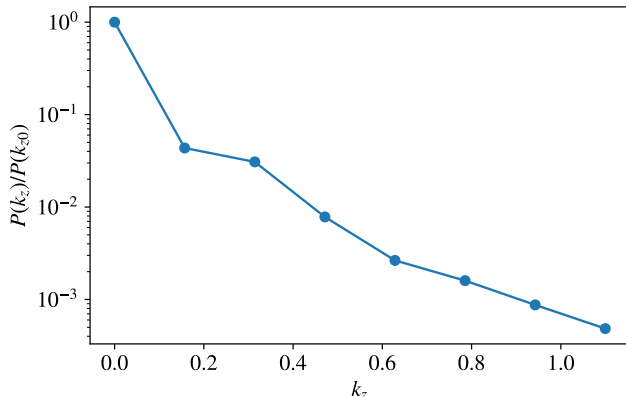


FIG. 16. Power in the Fourier transform in z of electron density fluctuations (averaged in x and y and from 10 to 16 ms). The power in the zeroth mode is at least ten times greater than the other modes, suggesting $k_z = 0$ is the dominant mode.

profiles. Since the experimental background density varies radially, a more accurate model would use the density-weighted Poisson equation, which includes the time and spatial variation in the ion guiding-center density on the left-hand side of the equation. Including a vertical $\mathbf{E} \times \mathbf{B}$ flow may account for some of the top-bottom asymmetry that is visible in the density equilibrium profiles. Other geometric features to include are magnetic shear and the radial variation in the connection length. These may affect where the transition from interchange to drift-wave turbulence occurs by giving the turbulence shorter parallel correlation length and breaking up the strong oscillatory dynamics present in the simulation.

A new, faster version of the Gkeyll code is being developed and will allow for scans in the ion-to-electron

mass ratio and collision frequencies to study their effect on turbulence statistics. Scans in connection length could also be performed to study the transition from interchange to drift-interchange turbulence. The physical and geometric features that we plan to include will be available in this version of the code. The effect of neutral particles is also significant in this parameter regime, and future development for the code will likely include an appropriate neutral model. Improvements to the conducting-sheath boundary conditions will also be considered.

ACKNOWLEDGMENTS

T.N.B. would like to thank F. Ebrahimi for reviewing the manuscript and for helpful discussions on turbulence spectra and convergence testing. This work used the Extreme Science and Engineering Discovery Environment (XSEDE), which is supported by National Science Foundation grant number ACI-1548562. We thank D.R. Hatch, J.M. Tenbarger, and F.L. Waelbroeck for contributing computational resources through their allocations on the Texas Advanced Computing Center Stampede2 cluster. We also thank J. Juno for helping set up Gkeyll on Stampede. This work was supported by the U.S. Department of Energy SCGSR program under contract DE-SC0014664, by DOE Contract DE-FG02-04ER-54742, through the Institute of Fusion Studies at the University of Texas at Austin, and DOE contract DE-AC02-09CH11466, through the Princeton Plasma Physics Laboratory (PPPL). G.W.H. and A.H. were supported in part by the SciDAC Partnership for Multiscale Gyrokinetics and the SciDAC Partnership for High-Fidelity Boundary Plasma Simulations. A.H. was also supported in part by the PPPL Laboratory Directed Research and Development program.

[1] T. Eich, A. Leonard, R. Pitts, W. Fundamenski, R. Goldston, T. Gray, A. Herrmann, A. Kirk, A. Kallenbach, O. Karadaun, A. Kukushkin, B. LaBombard, R. Maingi, M. Makowski, A. Scarabosio, B. Sieglin, J. Terry,

A. Thornton, ASDEX Upgrade Team, and JET EFDA Contributors, *Nucl. Fusion* **53**, 093031 (2013).

[2] R. Goldston, *Nucl. Fusion* **52**, 013009 (2012).

[3] S. I. Krasheninnikov, *Phys. Lett. A* **283**, 368 (2001).

- [4] S. Krasheninnikov, D. D'Ippolito, and J. Myra, *J. Plasma Phys.* **74**, 679 (2008).
- [5] S. Zweben and R. Gould, *Nucl. Fusion* **25**, 171 (1985).
- [6] S. Zweben, *Phys. Fluids* **28**, 974 (1985).
- [7] S. Zweben, R. Maqueda, D. Stotler, A. Keesee, J. Boedo, C. Bush, S. Kaye, B. LeBlanc, J. Lowrance, V. Mastrocola, *et al.*, *Nucl. Fusion* **44**, 134 (2003).
- [8] J. Terry, B. LaBombard, B. Lipschultz, M. Greenwald, J. Rice, and S. Zweben, *Fusion. Sci. Tech.* **51**, 342 (2007).
- [9] J. Boedo, J. Myra, S. Zweben, R. Maingi, R. Maqueda, V. Soukhanovskii, J. Ahn, J. Canik, N. Crocker, D. D'Ippolito, *et al.*, *Phys. Plasmas* **21**, 042309 (2014).
- [10] P. C. Stangeby, *The plasma boundary of magnetic fusion devices* (CRC Press, 2000).
- [11] M. Shimada, D. Campbell, V. Mukhovatov, M. Fujiwara, N. Kirneva, K. Lackner, M. Nagami, V. Pustovitov, N. Uckan, J. Wesley, N. Asakura, A. Costley, A. Donn, E. Doyle, A. Fasoli, C. Gormezano, Y. Gribov, O. Gruber, T. Hender, W. Houlberg, S. Ide, Y. Kamada, A. Leonard, B. Lipschultz, A. Loarte, K. Miyamoto, V. Mukhovatov, T. Osborne, A. Polevoi, and A. Sips, *Nucl. Fusion* **47**, S1 (2007).
- [12] A. Loarte, B. Lipschultz, A. Kukushkin, G. Matthews, P. Stangeby, N. Asakura, G. Counsell, G. Federici, A. Kallenbach, K. Krieger, *et al.*, *Nucl. Fusion* **47**, S203 (2007).
- [13] K. W. Gentle and H. He, *Plasma Sci. Tech.* **10**, 284 (2008).
- [14] J. C. Perez, W. Horton, K. Gentle, W. Rowan, K. Lee, and R. B. Dahlburg, *Phys. Plasmas* **13**, 032101 (2006).
- [15] F. Poli, S. Brunner, A. Diallo, A. Fasoli, I. Furno, B. Labit, S. Müller, G. Plyushchev, and M. Podestà, *Phys. Plasmas* **13**, 102104 (2006).
- [16] F. Poli, P. Ricci, A. Fasoli, and M. Podestà, *Phys. Plasmas* **15**, 032104 (2008).
- [17] P. Ricci, B. Rogers, and S. Brunner, *Phys. Rev. Lett.* **100**, 225002 (2008).
- [18] C. Williams, *Characterization of instability regimes in the Helimak, a simple magnetic torus*, *Ph.D. thesis*, UT Austin (2017).
- [19] B. Li, B. Rogers, P. Ricci, and K. Gentle, *Phys. Plasmas* **16**, 082510 (2009).
- [20] B. Li, B. Rogers, P. Ricci, K. Gentle, and A. Bhattacharjee, *Phys. Rev. E* **83**, 056406 (2011).
- [21] P. Ricci and B. Rogers, *Phys. Plasmas* **16**, 062303 (2009).
- [22] P. Ricci and B. Rogers, *Phys. Rev. Lett.* **104**, 145001 (2010).
- [23] K. Gentle, K. Liao, K. Lee, and W. Rowan, *Plasma Sci. Tech.* **12**, 391 (2010).
- [24] R. Cohen and X. Xu, *Contrib. Plasma Phys.* **48**, 212 (2008).
- [25] B. D. Scott, *Plasma Phys. Controlled Fusion* **45**, A385 (2003).
- [26] B. D. Scott, A. Kendl, and T. Ribeiro, *Contrib. Plasma Phys.* **50**, 228 (2010).
- [27] E. Shi, A. Hakim, and G. Hammett, *Phys. Plasmas* **22**, 022504 (2015).
- [28] E. Shi, G. Hammett, T. Stoltzfus-Dueck, and A. Hakim, *J. Plasma Phys.* **83**, 905830304 (2017).
- [29] E. Shi, *Gyrokinetic Continuum Simulation of Turbulence in Open-Field-Line Plasmas*, *Ph.D. thesis*, Princeton University (2017).
- [30] E. L. Shi, G. W. Hammett, T. Stoltzfus-Dueck, and A. Hakim, "Full- f gyrokinetic simulation of turbulence in a helical open-field-line plasma," (2018), [arXiv:1810.09500](https://arxiv.org/abs/1810.09500).
- [31] J.-G. Liu and C.-W. Shu, *J. Comput. Phys.* **160**, 577 (2000).
- [32] S. Gottlieb, C.-W. Shu, and E. Tadmor, *SIAM Rev.* **43**, 89 (2001).
- [33] M. A. Beer, S. C. Cowley, and G. Hammett, *Phys. Plasmas* **2**, 2687 (1995).
- [34] G. Hammett, M. Beer, W. Dorland, S. Cowley, and S. Smith, *Plasma Phys. Controlled Fusion* **35**, 973 (1993).
- [35] B. Scott, *Phys. Plasmas* **5**, 2334 (1998).
- [36] A. Mavrin, *J. Fusion Energ.* **36**, 161 (2017).
- [37] B. Li, X. Wang, C. Sun, C. Meng, A. Zhou, and D. Liu, *Phys. Plasmas* **24**, 055905 (2017).
- [38] M. Francisquez, B. Zhu, and B. Rogers, *Nucl. Fusion* **57**, 116049 (2017).
- [39] B. D. Dudson, J. Madsen, J. Omotani, P. Hill, L. Easy, and M. Løiten, *Phys. Plasmas* **23**, 062303 (2016).
- [40] F. Halpern, P. Ricci, S. Jolliet, J. Loizu, J. Morales, A. Mosetto, F. Musil, F. Riva, T.-M. Tran, and C. Wersal, *J. Comput. Phys.* **315**, 388 (2016).
- [41] P. Terry, *Rev. Mod. Phys.* **72**, 109 (2000).
- [42] B. Li, R. Hazeltine, and K. Gentle, *Phys. Rev. E* **76**, 066402 (2007).
- [43] N. Wiener, *Acta mathematica* **55**, 117 (1930).
- [44] A. Khintchine, *Mathematische Annalen* **109**, 604 (1934).
- [45] D. D'Ippolito, J. Myra, and S. Zweben, *Phys. Plasmas* **18**, 060501 (2011).